

Understanding External Pressure Effects and Interlayer Orbital Exchange Pathways in the Two-Dimensional Magnet—Chromium Triiodide

Ryan A. Beck, Shichao Sun, Xiaodong Xu, Daniel R. Gamelin, Ting Cao,* and Xiaosong Li*



Cite This: <https://doi.org/10.1021/acs.jpcc.2c03884>



Read Online

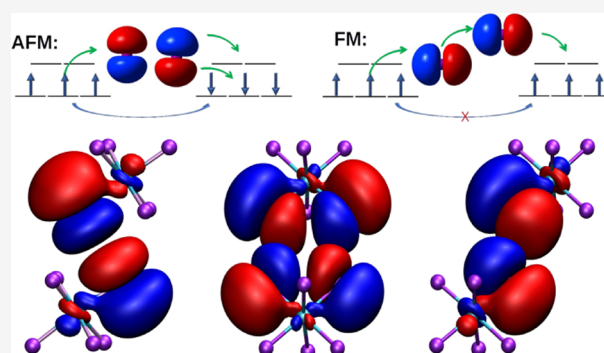
ACCESS |

Metrics & More

Article Recommendations

Supporting Information

ABSTRACT: Recent experiments have shown that exfoliated few-layer CrI₃, a prototypical van der Waals magnet, undergoes a phase transition from the high-temperature monoclinic structure to the low-temperature rhombohedral structure under pressure. To understand how the magnetism of CrI₃ responds to these structural changes, we perform ab initio density functional theory simulations on bilayer CrI₃. We simulate the interlayer lateral shift-dependent potential energy surface of bilayer CrI₃ to examine the stability and magnetism as a function of external pressure. Using the hybrid PBE0 functional, we are able to give qualitatively correct exchange coupling energies, without using an on-site Coulomb interaction correction. Thus, we avoid using tunable parameters. The results show that under external pressure, the monoclinic crystal structure is destabilized in comparison with the rhombohedral structure, in agreement with the observed phase transition in few-layer CrI₃ devices under pressure. We also look into the microscopic origins of the interlayer exchange coupling. We identify the competing orbital pathways that favor ferromagnetic and antiferromagnetic kinetic exchange, respectively, which are consistent with previous reports. This study opens a new direction of using hybrid functionals with Gaussian orbitals and a cluster-based approach for obtaining Heisenberg *J* values to accurately simulate the magnetic properties of 2D materials.



1. INTRODUCTION

Since 2D monolayer chromium triiodide (CrI₃) was first reported as having long-range magnetic order,¹ the origin of the anti-ferromagnetic interlayer exchange interaction in exfoliated few-layer structures has been of both experimental and theoretical interest. Ab initio simulations of the interlayer stacking and exchange interaction suggested that the antiferromagnetism arose in crystals with monoclinic stacking.^{2,3} Later, both second harmonic generation⁴ and polarization-resolved Raman spectroscopy⁵ showed that few-layer CrI₃ prepared by an exfoliation method maintained a monoclinic structure, even at low temperatures.⁶ This result is surprising since the bulk crystal will undergo a phase transition from monoclinic to rhombohedral stacking below ~200 K,^{7,8} which is well above the Curie temperature of 2D CrI₃ (*T*_c ≈ 45 K at the few-layer limit).¹ It was thus anticipated that at or below *T*_c, CrI₃ would thermodynamically favor rhombohedral stacking, so the observed monoclinic structures would be metastable. Indeed, recent experiments have found that the interlayer stacking of few-layer CrI₃ can be changed irreversibly by applying external pressure.^{6,9} Through the application of pressure, the stacking changes from monoclinic to rhombohedral, and the interlayer coupling also changes from antiferromagnetic to ferromagnetic.

Because CrI₃ has its magnetic moments localized on the Cr³⁺ ions, the Heisenberg model, given in eq 1, is often used to describe the exchange coupling, *J*_{*ij*}, between neighboring spin centers (*i* and *j*).

$$H = - \sum_{i,j>i} J_{ij} \mathbf{S}_i \cdot \mathbf{S}_j \quad (1)$$

where *S*_{*i*} is the total spin vector on the ion *i*. In this work, we focus primarily on the isotropic exchange coupling constant *J*_{*ij*} to identify the important ferromagnetic and antiferromagnetic interlayer coupling. Other important factors (e.g., single-ion anisotropy or anisotropic exchange) have not been included because they do not affect the qualitative discussion of the orbital pathways.^{10–18} Commonly, *J* is calculated using the four-state method^{19–21}

Received: June 4, 2022

Revised: October 24, 2022

$$J_{ij} = -\frac{E_{\uparrow\uparrow} - E_{\uparrow\downarrow} - E_{\downarrow\uparrow} + E_{\downarrow\downarrow}}{4S^2} \quad (2)$$

where all of the centers (beyond i and j) are held at a constant spin configuration for each of the four calculations, and each energy value, E_{ij} , corresponds to the center i or j having spins aligned either parallel (\uparrow) or antiparallel (\downarrow) to the magnetization axis. In order to avoid extraneous spin interactions in the periodic cells, a large supercell is required for the calculation. Previous ab initio work has examined the exchange coupling constant, J , between two Cr centers in molecular systems, and in these cases, the four-state method can be reduced to^{22–24}

$$J = -\frac{E_{\uparrow\uparrow} - E_{\uparrow\downarrow}}{2S^2} \quad (3)$$

This simplification is able to capture the majority of the $\text{Cr}^{3+}\text{--}\text{Cr}^{3+}$ coupling at a significantly reduced cost, primarily because calculations with a large supercell do not need to be performed.

The CrI_3 exchange coupling has been previously examined through the use of density functional theory (DFT), both at the collinear and noncollinear levels of theory (where the noncollinear approach includes spin–orbit coupling); however, these works suggest that the inclusion of spin–orbit coupling has little effect on the observed exchange coupling strength.^{10–18} These exchange coupling strengths are obtained by comparing ferromagnetic and antiferromagnetic states with the two different crystal stacking orders.^{3,5,25,26} It was concluded that the rhombohedral stacking has a ferromagnetic ground state, while the monoclinic stacking exhibits antiferromagnetic coupling. Competing orbital pathways favoring ferro- or antiferromagnetic coupling have been determined, with the overall magnetism of the 2D material depending on the relative strengths of the two.^{3,27}

In this work, we use cluster models to examine interlayer orbital exchange pathways in bilayer CrI_3 and how these pathways are modulated by translation and by external pressure to give insight into the experimental observations.

2. COMPUTATIONAL DETAILS

Many previous ab initio simulations of mono- and bilayer CrI_3 have used DFT at the local density approximation (LDA), generalized gradient approximation (GGA), LDA + U , or GGA + U level. As pointed out in a recent review (ref 18), simulating the magnetism of a 2D material is challenging for DFT because the interlayer magnetic exchange and magnetic anisotropy are small in energy and have distance-dependent mechanisms with competing effects on the observed magnetic properties; the interlayer interactions are dictated by the overlap between tails of atomic orbitals, which local density functionals struggle to describe. However, it has been shown that the magnetic exchange interaction calculated by GGA functionals is able to reproduce the antiferromagnetism of the monoclinic structure by adjusting on-site Coulomb corrections, U .^{18,25} Unfortunately, different values for correction parameters can change the sign and magnitude of this interlayer magnetic exchange coupling. Thus, careful tuning of the parameters is required, diminishing some of the appeals of ab initio approaches.^{3,26,28}

On the other hand, the importance of using hybrid functionals when examining magnetic properties has been noted.^{29,30} There have been previous reports of using either hybrid functionals with extended systems or even combining

hybrid functionals with Hubbard + U corrections to examine properties.^{31–35} Given that combining hybrid functionals and Hubbard + U terms still requires careful tuning of the + U parameters, in this work, we have chosen to use the hybrid exchange–correlation functional PBE0,^{36–38} without including the Hubbard U terms. We focus on studies of interlayer exchange coupling and orbital pathways in different crystal stackings at various interlayer distances. We also model the pressure-dependent magnetic behavior of bilayer CrI_3 that has been experimentally observed.^{6,9} Both cluster models and periodic Bloch functions composed of Gaussian-type orbitals are used in the Gaussian16 software package.³⁹ Periodic models are used in order to calculate the potential energy surfaces and to model the pressure-dependent properties of the high- and low-temperature structures. Cluster models are used to decipher the interplay between the Cr^{3+} centers between the layers. The Cr 3s, 3p, 3d, and 4s and I 5s and 5p electrons are explicitly treated with the valence double- ζ basis set, whereas the rest of the core electrons are modeled with the Los-Alamos pseudopotential (LANL2DZ).^{40–43}

3. EXCHANGE COUPLING ORBITAL PATHWAYS

Investigations into interlayer orbital exchange pathways in bilayer CrI_3 have been previously carried out in an attempt to explain the sign and mechanism of interlayer exchange coupling for the high- and low-temperature bilayer structures.^{3,27} In this work, we seek to provide additional insights into the dependence of exchange coupling on both lateral translation and external pressure on the same footing. The strength of a superexchange pathway is related to the overlap of the ligand orbitals with those of the magnetic ion.⁴⁴ To see how the stacking geometries affect the orbital pathways and thus the magnetic exchange, orbitals for each type of $\text{Cr}^{3+}\text{--}\text{Cr}^{3+}$ pair are examined. The orbital pathways are studied for the closest, second, and third nearest interlayer Cr^{3+} neighbors in the high-temperature monoclinic structure, built by choosing the relevant interlayer $[\text{CrI}_6]^{3-}$ ion pairs to form a $[\text{Cr}_2\text{I}_{12}]^{6-}$ cluster as shown in Figure 1, with geometric parameters shown in Figure 2. The computed exchange coupling strengths are listed in Table 1. Although the following discussion will mainly focus on the orbital pathways in the monoclinic structure, the general conclusion is similar for the rhombohedral structure. In Table 2, we also list the exchange coupling strengths for the rhombohedral structure for comparison.

In the pseudo-octahedral crystal field of CrI_3 , the Cr^{3+} d manifold splits into triply degenerate t_{2g} and doubly degenerate e_g orbitals, as shown in Figure 3, with the three t_{2g} orbitals each occupied with one unpaired electron. Antiferromagnetic (AFM) exchange allows the delocalization of $\text{Cr}^{3+}(t_{2g})$ electrons into both the t_{2g} and e_g orbitals of another Cr^{3+} center, whereas the ferromagnetic (FM) pathway allows $\text{Cr}^{3+}(t_{2g}) \rightarrow \text{Cr}^{3+}(e_g)$ delocalization due to Pauli exclusion. Such delocalization often favors antiferromagnetic coupling, but the relative strengths of ferromagnetic and antiferromagnetic pathways can be modulated through different alignments of the mediating orbitals (e.g., $\Gamma(p)$ orbitals).

Each $\text{Cr}^{3+}\text{--}\text{Cr}^{3+}$ pair has both ferromagnetic and antiferromagnetic exchange pathways, mediated by different groups of $\Gamma(p)$ orbitals (see Figure 3). In these pathways, the $\text{Cr}^{3+}(t_{2g})$ orbitals first interact with $\Gamma(p)$ orbitals on the coordinating iodide. These $\Gamma(p)$ orbitals then weakly interact

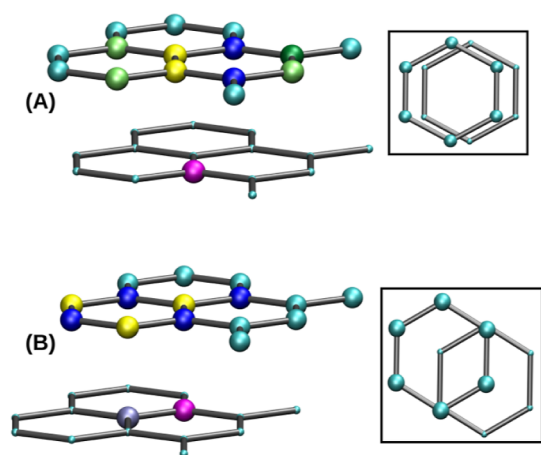


Figure 1. (A) (Left) Neighboring interlayer Cr^{3+} pairs of the high-temperature structure. The nearest-neighbor Cr^{3+} ions to the bottom-layer (magenta) Cr^{3+} are in yellow, the second nearest neighbors are in dark blue, and the third nearest neighbors are in green. Two different colors for the third nearest neighbors are shown in light green corresponding to the third nearest (I) and in dark green corresponding to the third nearest (II) from Table 1. (Right) A top-down view of the CrI_3 high-temperature lattice with the top layer containing explicit Cr^{3+} atoms, and the bottom layer is shown as tubes. (B) (Left) Neighboring interlayer Cr^{3+} pairs of the low-temperature structure. The top-layer Cr^{3+} ions corresponding to the nearest (I) and nearest (II) pairs (shown in Table 2) are shown in yellow and are paired with the magenta and gray bottom-layer Cr^{3+} ions, respectively. The second nearest neighbors are in dark blue. (Right) A top-down view of the low-temperature CrI_3 lattice with the top layer containing explicit Cr^{3+} atoms, and the bottom layer is shown as tubes.

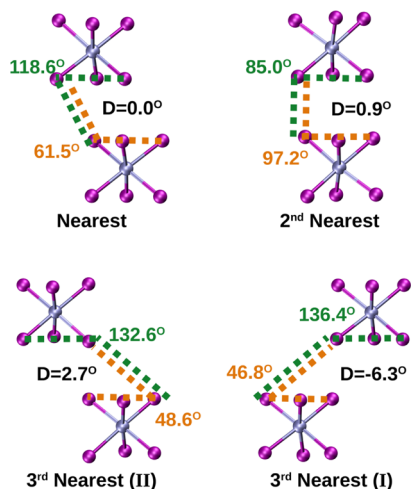


Figure 2. Angles between the bridging I_4 groups of the $[\text{Cr}_2\text{I}_{12}]^{6-}$ pairs featured in Table 1. Displayed are the Cr^{3+} ions (blue) in the octahedron of the I^- anions (purple). Colored dashed lines, and the accompanying colored numbers, indicate the angles between marked I^- ions.

with $\text{I}^-(\text{p})$ orbitals on the adjacent layer, which provide a pathway to the Cr^{3+} center in the second layer. Through such a pathway, the d electrons are slightly delocalized across layers, giving rise to the preferred interlayer magnetic alignment. The two dominant interlayer paths are visualized by plotting differences in charge density between the ferro- and antiferromagnetic states, as shown in Figures 4A, 5A, and

Table 1. Coupling Strengths of Nearest-Neighbor $[\text{Cr}_2\text{I}_{12}]^{6-}$ Clusters in the High-Temperature Monoclinic Structure^a

neighbor	$\text{Cr}^{3+}-\text{Cr}^{3+}$ distance (Å)	J (meV)
nearest	6.984	0.615
	7.020	0.572
	8.028	-0.692
Second nearest	8.092	-0.520
	8.929	0.072
Third nearest (I)	8.981	0.039
	8.981	0.033
	9.008	0.116

^aNeighbor pairs that can be visualized in Figure 2 are bolded.

Table 2. Coupling Strengths of Nearest-Neighbor $[\text{Cr}_2\text{I}_{12}]^{6-}$ Clusters in the Low-Temperature Rhombohedral Structure^a

neighbor	$\text{Cr}^{3+}-\text{Cr}^{3+}$ distance (Å)	J (meV)
nearest (I)	6.589	0.272
nearest (II)	7.701	0.587
Second nearest	7.713	0.532

^aNeighbor pairs that can be visualized in Figure 2 are bolded.

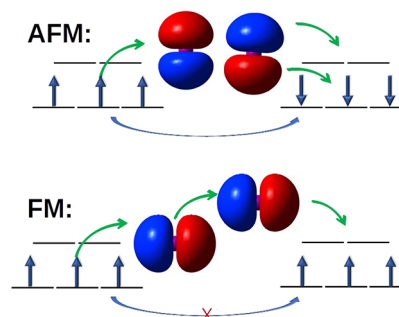


Figure 3. Schematic of allowed kinetic exchange pathways coupling two Cr^{3+} ions from different CrI_3 layers (valence d orbitals split by the octahedral ligand field), mediated by I^- ligands, showing (on top) the chromium direct exchange (blue arrow, allowed in AFM) and the ligand-mediated superexchange (green) pathways. The bottom scheme shows that direct exchange is forbidden in the FM case.

6A. This difference in total density can be used to help identify the key orbitals involved in the exchange pathway. In addition, representative molecular orbitals (MOs) for these interactions are plotted and analyzed.

In the case of ferromagnetic exchange for the interlayer nearest-neighbor (shown in Figure 4B), the $\text{Cr}^{3+}(e_g)$ orbital has σ -type interactions with the coordinated $\text{I}^-(\text{p})$ orbitals. There is one pair of interlayer iodide ions through which the majority of the interaction takes place. The p orbitals on these ions have a σ^* -type interaction between them. The second-layer iodide then interacts via a σ -type overlap with the e_g orbital of Cr^{3+} in the second layer. This state is a “virtual state”, as has been noted to occur in ref 17, which allows the interactions between the filled t_{2g} and e_g orbitals. In the ferromagnetic case, this results in the Cr^{3+} ions showing the e_g character that can be noted in Figure 4B,C. In the antiferromagnetic orbital pathway (Figure 4C), the $\text{Cr}^{3+}(t_{2g})$ orbital has π interactions with the coordinated $\text{I}^-(\text{p})$ orbital. This I^- -p orbital then interacts in a similar manner to the ferromagnetic pathway where the two iodide ions have a σ^* -type interaction and the $\text{Cr}^{3+}(e_g)$ and $\text{I}^-(\text{p})$ orbitals on the second layer have a σ -type interaction. Thus, the $\text{Cr}^{3+}(\text{d})$

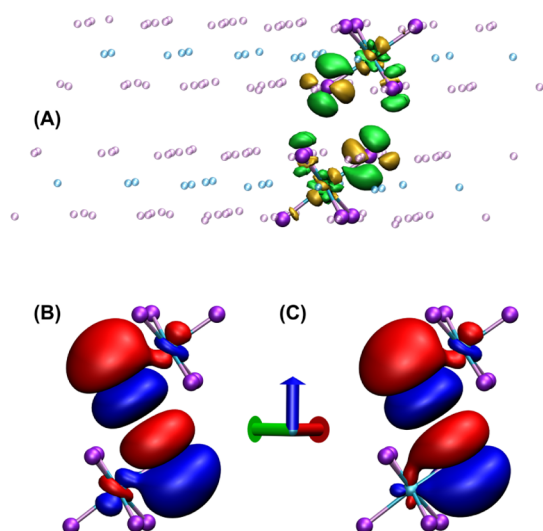


Figure 4. Nearest-neighbor $[\text{Cr}_2\text{I}_{12}]^{6-}$ cluster. Cr^{3+} ions are shown in blue, and I^- anions are shown in purple. (A) Plots of difference in total density (FM–AFM) showing the different interactions between the centers, FM (yellow) and AFM (green), plotted with an isovalue of 4×10^{-5} electrons/ Bohr^3 . The $[\text{Cr}_2\text{I}_{12}]^{6-}$ pair is displayed in a virtual background of the CrI_3 bilayer structure. (B) Contributions to the HOMO of the FM-ordered Cr^{3+} ions by the significant atoms for the exchange determined in (A), with (C) for the AFM-ordered Cr^{3+} ions, plotted with an isovalue of 0.01 electrons/ Bohr^3 . Spin densities for both FM and AFM solutions can be found in the [Supporting Information](#).

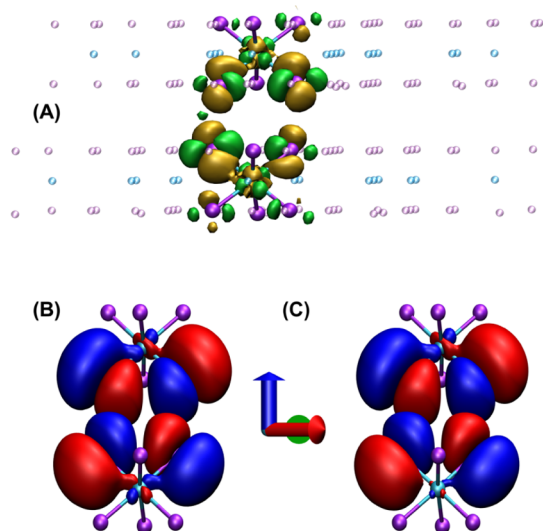


Figure 5. Second nearest-neighbor $[\text{Cr}_2\text{I}_{12}]^{6-}$ cluster. Cr^{3+} ions are shown in blue, and I^- ions are shown in purple. (A) Plots showing the difference in total density (FM–AFM) showing the different interactions between the centers, FM (yellow) and AFM (green), plotted with an isovalue of 4×10^{-5} electrons/ Bohr^3 . The $[\text{Cr}_2\text{I}_{12}]^{6-}$ pair is displayed in a virtual background of the CrI_3 bilayer structure. (B) Contributions to the HOMO of the FM-ordered Cr^{3+} ions by the significant atoms for the exchange determined in (A), with (C) for the AFM-ordered Cr^{3+} ions, and are plotted with an isovalue of 0.01 electrons/ Bohr^3 . Spin densities for both FM and AFM solutions can be found in the [Supporting Information](#) (Figure S2).

orbitals from the two layers are coupled together, resulting in another “virtual state”; however, since the spins on the Cr^{3+}

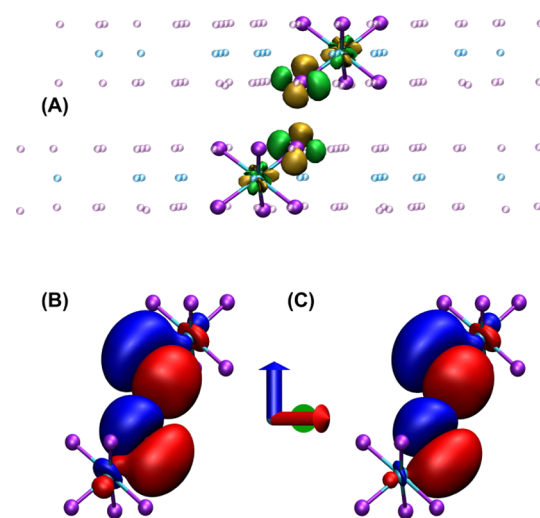


Figure 6. Third nearest-neighbor $[\text{Cr}_2\text{I}_{12}]^{6-}$ cluster. Cr^{3+} ions are shown in blue, and I^- ions are shown in purple. (A) Plots of the difference in total density (FM–AFM) showing the different interactions between the centers, FM (yellow) and AFM (green), plotted with an isovalue of 4×10^{-5} electrons/ Bohr^3 . The $[\text{Cr}_2\text{I}_{12}]^{6-}$ pair is displayed in a virtual background of the CrI_3 bilayer structure. (B) Contributions to the HOMO of the FM-ordered Cr^{3+} ions by the significant atoms for the exchange determined in (A), with (C) for the AFM-ordered Cr^{3+} ions plotted with an isovalue of 0.01 electrons/ Bohr^3 . Spin densities for both FM and AFM solutions can be found in the [Supporting Information](#).

ions are opposing, only one e_g orbital is present (going from spin-up to spin-down orbital visualization, the Cr^{3+} ion presenting e_g orbital character changes). This antiferromagnetic pathway is weaker than the ferromagnetic one, resulting in the closest $[\text{Cr}_2\text{I}_{12}]^{6-}$ pair exhibiting a ferromagnetically coupled ground state (J value of 0.572 meV, given in [Table 1](#)).

For the second nearest-neighbor interlayer pair, the orbital pathways are shown in [Figure 5A](#). In this case, the difference between the ferro- and antiferromagnetic pathway through the I^- ions is clearer than in the nearest-neighbor case. The ferromagnetic exchange pathway involves σ -type interactions between the bridging I^- ions, while the antiferromagnetic ordering can be seen to have more π -type character. On examining [Figure 5B,C](#), we can see that the Cr–I interactions are not as clear as in the nearest-neighbor case. It is interesting to note that for the ferromagnetic pathway ([Figure 5B](#)), the virtual state for the nearest-neighbor case is less prominent and appears to be closer to the antiferromagnetic pathway (t_{2g} to e_g mediated by I^- ions). This inability to fully realize the ferromagnetic pathway manifests in an antiferromagnetic ordering for the pairs.

The third nearest-neighbor interlayer pairs have similar interactions. An orbital figure for one of the third nearest-neighbor (type I) interactions is provided in [Figure 6](#). The I^- ion interactions look very similar to those of the second nearest-neighbor pair, where the ferromagnetic pathway involves an I^- – I^- σ -type character and the antiferromagnetic pathway involving a π -type interaction. Unlike the second nearest neighbor, however, these interactions are only facilitated by a single I^- pair, similar to that of the nearest neighbor. In addition, the Cr^{3+} – I^- interactions can be seen to behave like the nearest-neighbor pairs. The coupling reflects this similarity, with both third nearest-neighbor pairs coupled

ferromagnetically at zero pressure, although much weaker than the first or second nearest-neighbor pairs (J value of 0.039 and 0.116 meV for third nearest-neighbors type I and type-II, respectively, given in Table 1). As the Cr^{3+} – Cr^{3+} distance increases beyond the third nearest-neighbor pair, the magnetic exchange coupling between Cr^{3+} centers becomes negligible.

Overall, this analysis suggests that the high-temperature crystal should show antiferromagnetic interlayer coupling, dominated by the antiferromagnetically coupled second nearest-neighbor pairs. Because the strength of each magnetic exchange pathway between two Cr^{3+} centers is highly dependent on the geometry of the intervening iodide ions, the trend of the net magnetic coupling strength does not simply decay as the internuclear distance increases, as shown in Tables 1 and 2. Depending on the relative strengths of the anti- and ferromagnetic pathways for a given geometry, the monoclinic and rhombohedral structures can exhibit different magnitudes and sometimes different signs of the net magnetic coupling. Because the monoclinic and rhombohedral structures are related by a translation along the xy plane, we will examine how the lateral translation can modulate the exchange coupling.

4. DEPENDENCE OF EXCHANGE COUPLING ON LATERAL TRANSLATION

We first use lateral translation scans at the fixed crystal interlayer distance to study the relationship of the stacking structure and exchange interaction. In contrast to the cluster models used in the previous section to study orbital pathways, calculations in this section are carried out using periodic Bloch functions composed of Gaussian-type orbitals with the low-temperature rhombohedral structure as the starting point (0.0, 0.0). Similar rigid scans at the crystal lattice distance have been previously studied using pure GGA functionals and showed that the magnetic character of the bilayer structure depends on the lateral translation.²⁵ Initial bilayer geometries for the translation scan are taken from the experimentally measured bulk low-temperature rhombohedral crystal structure.⁷ The bottom layer of the periodic system is fixed and the upper layer is translated in x and y (where z is perpendicular to the CrI_3 plane) along the lattice vectors in a 20×20 point grid from $-a + b/2$ to $a + b/2$, where a and b are the edge lengths of the unit cell. The lateral translation vectors to go from rhombohedral to monoclinic stacking are listed in Table 3.

In Figure 7A, we present potential energy surfaces for the ferromagnetically coupled bilayer CrI_3 under lateral translation at an interlayer distance of 6.60 Å. The potential energy surface (Figure 7A) has been scaled by the energy of the

Table 3. Translation Vector of Lateral Translation from Rhombohedral to Monoclinic

monoclinic structure	translation vector with $a = 6.867$ Å
1	$(-a/3, 0) = (-2.289, 0.0)$
2	$\left(\frac{a}{6}, \frac{\sqrt{3}a}{6}\right)$ $= (1.145, 1.982)$
3	$\left(\frac{a}{6}, -\frac{\sqrt{3}a}{6}\right)$ $= (1.145, -1.982)$

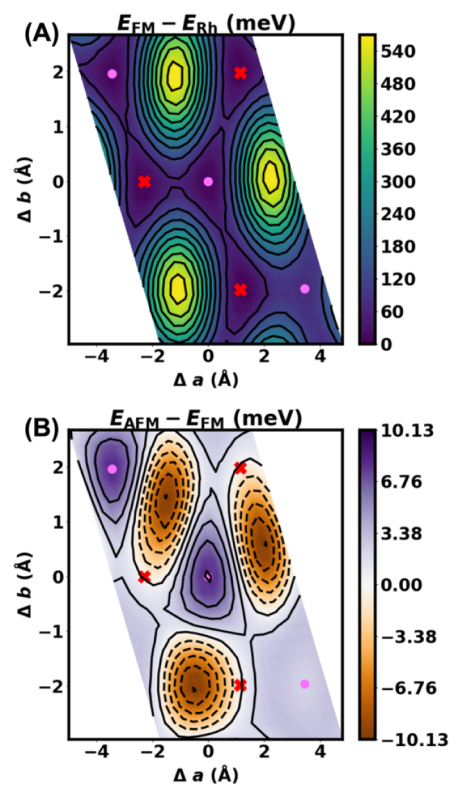


Figure 7. Lateral translation scan of a bilayer CrI_3 crystal at the crystal interlayer distance (6.60 Å). (A) Energy (in meV per unit cell) of the ferromagnetic configuration (E_{FM}) of the translated crystal in relation to the central, rhombohedral structure (0.0, 0.0), E_{Rh} . The three magenta circles mark rhombohedral crystal structures, and the red crosses denote the monoclinic crystal structures as given in Table 3. (B) Difference in energy between the anti- and ferromagnetic configurations (AFM–FM in meV per unit cell). This result shows that the rhombohedral structure has a FM ground state, while the surrounding monoclinic structures exhibit interlayer antiferromagnetism.

rhombohedral geometry to aid in the analysis of the geometric surface, and shows that the rhombohedral crystal structure at the central coordinate (0.0, 0.0) is the energetic global minimum. This is the low-temperature thermodynamically preferred structure. The three surrounding energetic local minima, corresponding to the high-temperature monoclinic structures, are marked with red crosses and are 0.90 meV higher in energy than the rhombohedral structure when ferromagnetic coupling is retained.

Figure 7B examines the magnetic character of the various structures. It shows that the ferromagnetic configuration of the energetic global minimum (rhombohedral structure) is lower in energy than the antiferromagnetic state. However, the local minima (monoclinic structure marked with red crosses) can be seen to be within the antiferromagnetic regime, which suggests that the lateral translation from the rhombohedral to monoclinic structure is associated with a transition from ferromagnetic to antiferromagnetic interlayer coupling, consistent with experiment.

5. PRESSURE-DEPENDENT EXCHANGE COUPLING

The relationship between interlayer distance and exchange coupling strength has generated some debate in recent theoretical studies. Simulation with pure GGA functionals

shows that the bilayer high-temperature monoclinic structure with applied pressure results in ferromagnetic interlayer coupling at shorter interlayer distances, and as the interlayer distance increases, the antiferromagnetic state becomes lower in energy than the ferromagnetic configuration.²⁶ For the low-temperature rhombohedral structure, the change in interlayer distance does not result in a change of the interlayer magnetic coupling, and the electronic ground state remains ferromagnetic.²⁶ In another theoretical study, it was noted that the FM to AFM change was due to the tensile strain of the CrI₃ layers, and the magnetic phase was not found to be affected by vertical compression of the CrI₃ layers.¹⁶

To better understand the changes in few-layer CrI₃ under external pressure observed in experiments,^{6,9} we perform lateral translation scans at different interlayer distances for bilayer CrI₃. From the potential energy surfaces generated by rigid scans at different interlayer distances, we seek to understand the mechanism of phase transition under external pressure. Figure 8 shows potential energy surfaces obtained from lateral translation scans of the CrI₃ bilayers at various interlayer distances shorter than in the equilibrium rhombohedral structure. Figure 8A,C shows that the rhombohedral crystal structure (0.0, 0.0) is still the most stable, with a ferromagnetic ground state character. The total energy potential energy surface (Figure 8A,C) has been scaled by the energy of the rhombohedral geometry to aid in the analysis of the geometric surface. The three monoclinic local minima are antiferromagnetic. At the equilibrium interlayer distance of 6.60 Å, the difference in energy between the ferromagnetic rhombohedral and ferromagnetic monoclinic configurations is 0.90 meV per unit cell. Upon applying pressure, this energetic difference increases markedly to 372 meV per unit cell at a 5.60 Å interlayer distance. Figure 8B,D shows that as the interlayer distance decreases, the ferromagnetic configuration at the rhombohedral structure and the antiferromagnetic configuration at the monoclinic structure both are stabilized. In addition, the antiferromagnetic domain seems to enlarge as the pressure increases. This can be seen in Figures 7B and 8B,D as the spatial extent of the antiferromagnetic character increases with increasing pressure.

Figure 9 plots the magnetism as a function of the translation *a* vector while keeping the *b* vector fixed at 0.0. It is clear that the shorter interlayer distance leads to the increasing stabilization of the antiferromagnetic configuration of the monoclinic structure and of the ferromagnetic configuration of the rhombohedral structure. This observation agrees with the experiment, where it was found that the antiferromagnetic state becomes more stable until the crystal reorganizes to the low-temperature rhombohedral structure.^{6,9}

Figure 10A shows that as the pressure increases, the rhombohedral structure becomes more stable. Thus, the crystal can go through a lateral translation from a monoclinic structure to rhombohedral to obtain a thermodynamically more stable structure under enough pressure. Figure 10B shows that when the layers are too far apart, they do not interact ($E_{AFM} - E_{FM}$ approaches zero). However, as they get closer, the monoclinic and rhombohedral structures behave differently. While the rhombohedral structure starts as ferromagnetic and grows increasingly ferromagnetic as the layers get closer, the monoclinic structure becomes increasingly antiferromagnetic. The two structures have a difference in the rate at which the exchange coupling strength grows, where $|E_{AFM} - E_{FM}|$ of the rhombohedral structure grows much more

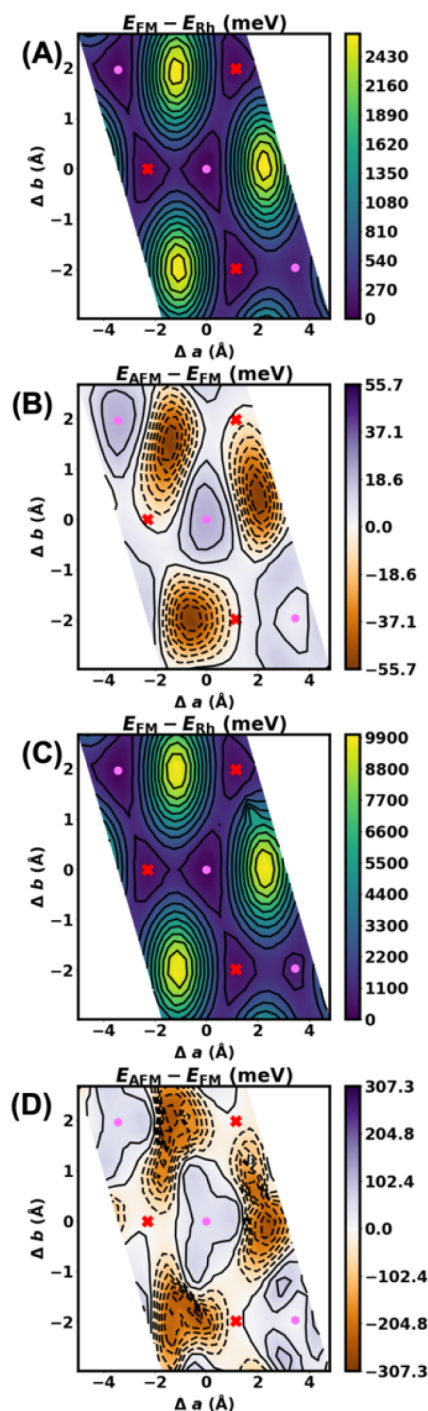


Figure 8. Lateral translation of the CrI₃ bilayer structures, where the interlayer distances are $d = 6.10$ Å (A,B) and $d = 5.60$ Å (C,D). (A,C) show the energy of the ferromagnetic system (E_{FM}) above the rhombohedral structure (E_{Rh} in meV per unit cell) located at (0.0, 0.0). (B,D) show the difference in energies between the antiferromagnetic and ferromagnetic states (in meV per unit cell). As in Figure 7, the three magenta circles mark rhombohedral crystal structures, while the red crosses mark monoclinic crystal structures. Please note the changing energy scale.

rapidly than that for the monoclinic structure. This effect has been also observed previously in other *ab initio* works.²⁶

Since the rhombohedral structure always exhibits ferromagnetic coupling, as the crystal undergoes a structural transformation from a monoclinic to rhombohedral structure, the

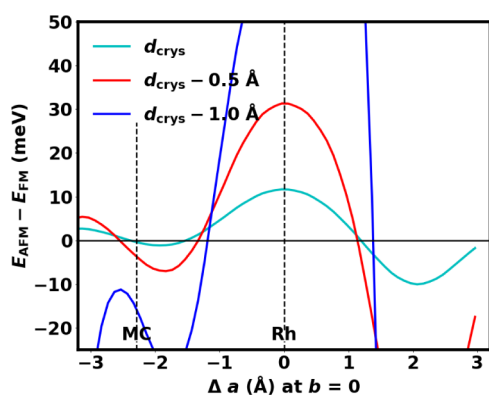


Figure 9. Difference in energy between the anti- and ferromagnetic states as a function of the transnational a vector while keeping the b vector fixed at 0.0 for the three interlayer distances, $d = 6.60$, $d = 6.10$, and $d = 5.60$. Vertical dashed lines mark the monoclinic structure (MC at -2.289) and rhombohedral structure (Rh at 0.000).

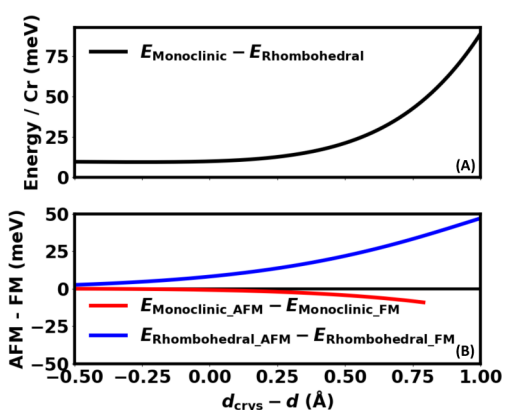


Figure 10. (A) Difference in energy (in meV per Cr atom) of the ferromagnetically coupled monoclinic and rhombohedral structures. (B) Difference in energy between the FM and AFM states (in meV per unit cell) for monoclinic and rhombohedral structures as a function of pressure.

magnetism of the crystal will change from AFM to FM with applied pressure. This effect has been experimentally observed in refs 6 and 9.

Figure 11 shows how exchange coupling for select interlayer neighboring Cr^{3+} – Cr^{3+} pairs in the monoclinic and rhombohedral structures change as a function of external pressure. As the Cr^{3+} ions get closer, their magnetic coupling strength increases. The second-nearest-neighbor coupling of the monoclinic structure is the most responsive to the deformation as the two Cr centers are close enough to each other to interact closely and are able to strongly favor the antiferromagnetic pathway. The nearest neighbors have strongly competing AFM and FM pathways which act to limit the magnitude of the exchange, and the third nearest neighbors are too distant to have as strong an interaction. It is interesting to see that in the monoclinic structure, the nearest neighbor and third nearest neighbor(II) become increasingly ferromagnetic. These gains, however, are not enough to compete with the drastic increases in antiferromagnetic exchange of the second-nearest-neighbor and third nearest-neighbor(I) pairs, giving rise to the observed increasing antiferromagnetism of the bilayer monoclinic systems. This effect is notably absent in the rhombohedral structure, where all pairs only exhibit ferromagnetic coupling,

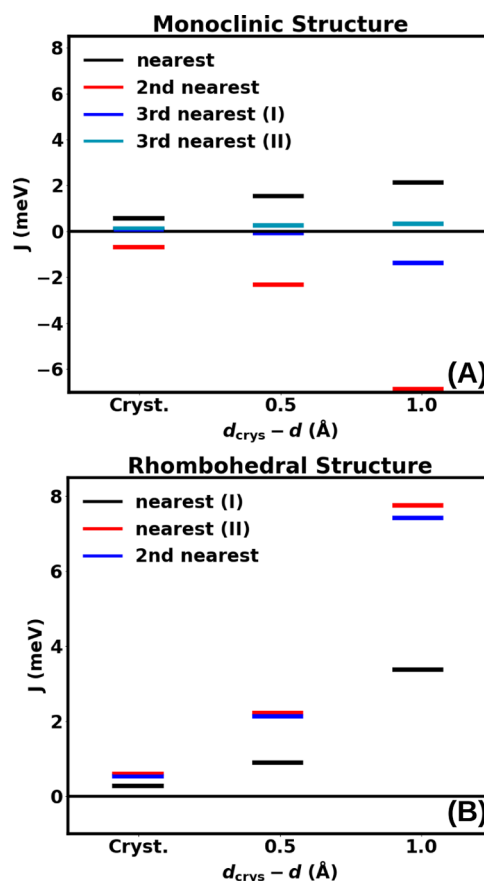


Figure 11. J values for the selected monoclinic (A) and rhombohedral (B) Cr pairs given in Tables 1 and 2, respectively.

and it may be one of the reasons the growth of $|E_{\text{AFM}} - E_{\text{FM}}|$ is different in the rhombohedral and monoclinic phases.

6. CONCLUSIONS

In summary, we studied bilayer 2D CrI_3 with periodic ab initio simulations at a hybrid functional level of theory with atom-centered basis. Qualitatively, correct magnetic exchange energies are obtained without using on-site Coulomb interactions of localized electrons or using additional Hubbard-like terms. It was shown that coupling values calculated for select Cr^{3+} – Cr^{3+} pairs are able to provide insights into the magnetism of CrI_3 at significantly reduced cost in comparison to the more rigorous four-state method. The mechanism for an observed change in magnetic coupling from FM to antiferromagnetic with pressure was examined through lateral translation scans at different interlayer distances to simulate various external pressures. It was determined that the rhombohedral crystal structure is more energetically stable and is destabilized less under pressure in comparison to the monoclinic structure. As pressure is applied, however, interlayer coupling increases, resulting in greater antiferromagnetic interlayer coupling in monoclinic CrI_3 and greater ferromagnetic coupling in rhombohedral CrI_3 . This observation echoes what has been observed experimentally for few-layer CrI_3 under pressure.

Although rigid scans were used in this work for the analysis of the magnetic exchange pathways under external pressure, it is not expected that relaxed scans will significantly alter the observed magnetic properties or the fundamental orbital

exchange pathways. Also additional factors not explored in this work, such as dispersion, may play a role in the optimized interlayer distance.

This work has provided important insights, showing that magnetic coupling in the monoclinic crystal is dominated by the second-nearest-neighbor Cr^{3+} ions, which drive the antiferromagnetic interlayer coupling. This situation differs from the rhombohedral crystal in which all Cr^{3+} – Cr^{3+} pairs exhibit ferromagnetic interlayer coupling, resulting in the magnitude of interlayer coupling being greater for the rhombohedral CrI_3 . These insights will be helpful for future design of devices utilizing these materials.

■ ASSOCIATED CONTENT

SI Supporting Information

The Supporting Information is available free of charge at <https://pubs.acs.org/doi/10.1021/acs.jpcc.2c03884>.

Empirical dispersion, clarification of the pressures examined, and spin densities for select Cr^{3+} pairs (PDF)

■ AUTHOR INFORMATION

Corresponding Authors

Ting Cao – Department of Materials Science and Engineering, University of Washington, Seattle, Washington 98195, United States; orcid.org/0000-0003-1300-6084; Email: tingcao@uw.edu

Xiaosong Li – Department of Chemistry, University of Washington, Seattle, Washington 98195, United States; orcid.org/0000-0001-7341-6240; Email: xsli@uw.edu

Authors

Ryan A. Beck – Department of Chemistry, University of Washington, Seattle, Washington 98195, United States; orcid.org/0000-0002-2953-970X

Shichao Sun – Department of Chemistry, University of Washington, Seattle, Washington 98195, United States; orcid.org/0000-0002-7680-3972

Xiaodong Xu – Department of Physics, University of Washington, Seattle, Washington 98195, United States; orcid.org/0000-0003-0348-2095

Daniel R. Gamelin – Department of Chemistry, University of Washington, Seattle, Washington 98195, United States; orcid.org/0000-0003-2888-9916

Complete contact information is available at: <https://pubs.acs.org/10.1021/acs.jpcc.2c03884>

Notes

The authors declare no competing financial interest.

■ ACKNOWLEDGMENTS

The study of two-dimensional magnetic materials was supported by the University of Washington Molecular Engineering Materials Center (DMR-1719797). X.L. acknowledges the support from the National Science Foundation (CHE-2154346) for developing theories to investigate magnetic properties. This work was facilitated through the use of advanced computational, storage, and networking infrastructure provided by the Hyak supercomputer system and funded by the STF at the University of Washington. Figures ¹, ², and ^{4–6} are plotted using VMD.⁴⁵

■ REFERENCES

- (1) Huang, B.; Clark, G.; Navarro-Moratalla, E.; Klein, D. R.; Cheng, R.; Seyler, K. L.; Zhong, D.; Schmidgall, E.; McGuire, M. A.; Cobden, D. H.; Yao, W.; Xiao, D.; Jarillo-Herrero, P.; Xu, X. Layer-Dependent Ferromagnetism in a van der Waals Crystal Down to the Monolayer Limit. *Nature* **2017**, *546*, 270–273.
- (2) Wang, Z.; Gutiérrez-Lezama, I.; Ubrig, N.; Kroner, M.; Gibertini, M.; Taniguchi, T.; Watanabe, K.; Imamoğlu, A.; Giannini, E.; Morpurgo, A. F. Very Large Tunneling Magnetoresistance in Layered Magnetic Semiconductor CrI_3 . *Nat. Commun.* **2018**, *9*, 2516.
- (3) Jiang, P.; Wang, C.; Chen, D.; Zhong, Z.; Yuan, Z.; Lu, Z.-Y.; Ji, W. Stacking tunable interlayer magnetism in bilayer CrI_3 . *Phys. Rev. B* **2019**, *99*, 144401.
- (4) Sun, Z.; Yi, Y.; Song, T.; Clark, G.; Huang, B.; Shan, Y.; Wu, S.; Huang, D.; Gao, C.; Chen, Z.; McGuire, M.; Cao, T.; Xiao, D.; Liu, W.-T.; Yao, W.; Xu, X.; Wu, S. Giant nonreciprocal second-harmonic generation from antiferromagnetic bilayer CrI_3 . *Nature* **2019**, *572*, 497–501.
- (5) Ubrig, N.; Wang, Z.; Teyssier, J.; Taniguchi, T.; Watanabe, K.; Giannini, E.; Morpurgo, A. F.; Gibertini, M. Low-temperature monoclinic layer stacking in atomically thin CrI_3 crystals. *2D Mater.* **2019**, *7*, 015007.
- (6) Song, T.; Fei, Z.; Yankowitz, M.; Lin, Z.; Jiang, Q.; Hwangbo, K.; Zhang, Q.; Sun, B.; Taniguchi, T.; Watanabe, K.; McGuire, M. A.; Graf, D.; Cao, T.; Chu, J.-H.; Cobden, D. H.; Dean, C. R.; Xiao, D.; Xu, X. Switching 2D Magnetic States via Pressure Tuning of Layer Stacking. *Nat. Mater.* **2019**, *18*, 1298–1302.
- (7) McGuire, M. A.; Dixit, H.; Cooper, V. R.; Sales, B. C. Coupling of Crystal Structure and Magnetism in the Layered, Ferromagnetic Insulator CrI_3 . *Chem. Mater.* **2015**, *27*, 612–620.
- (8) McGuire, M. A.; Dixit, H.; Cooper, V. R.; Sales, B. C. Coupling of Crystal Structure and Magnetism in the Layered, Ferromagnetic Insulator CrI_3 . *Compos. Mater.* **2015**, *27*, 612–620.
- (9) Li, T.; Jiang, S.; Sivadas, N.; Wang, Z.; Xu, Y.; Weber, D.; Goldberger, J. E.; Watanabe, K.; Taniguchi, T.; Fennie, C. J.; Fai Mak, K.; Shan, J. Pressure-controlled interlayer magnetism in atomically thin CrI_3 . *Nat. Mater.* **2019**, *18*, 1303–1308.
- (10) Lado, J. L.; Fernández-Rossier, J. On the origin of magnetic anisotropy in two dimensional CrI_3 . *2D Mater.* **2017**, *4*, 035002.
- (11) Zhang, W.-B.; Qu, Q.; Zhu, P.; Lam, C.-H. Robust Intrinsic Ferromagnetism and Half Semiconductivity in Stable Two-Dimensional Single-Layer Chromium Trihalides. *J. Mater. Chem. C* **2015**, *3*, 12457–12468.
- (12) Kashin, I.; Mazurenko, V.; Katsnelson, M.; Rudenko, A. Orbitaly-resolved ferromagnetism of monolayer CrI_3 . *2D Mater.* **2020**, *7*, 025036.
- (13) Torelli, D.; Olsen, T. Calculating Critical Temperatures for Ferromagnetic Order in Two-Dimensional Materials. *2D Mater.* **2018**, *6*, 015028.
- (14) Besbes, O.; Nikolaev, S.; Meskini, N.; Solov'yev, I. Microscopic origin of ferromagnetism in the trihalides CrCl_3 and CrI_3 . *Phys. Rev. B* **2019**, *99*, 104432.
- (15) Xu, C.; Feng, J.; Xiang, H.; Bellaiche, L. Interplay between Kitaev Interaction and Single Ion Anisotropy in Ferromagnetic CrI_3 and CrGeTe_3 Monolayers. *npj Comput. Mater.* **2018**, *4*, 57.
- (16) León, A.; González, J.; Mejía-López, J.; Crasto de Lima, F. C.; Suárez Morell, E. S. Strain-induced phase transition in CrI_3 bilayers. *2D Mater.* **2020**, *7*, 035008.
- (17) Jiang, Y.; Guo, Y.; Yan, X.; Zeng, H.; Lin, L.; Mou, X. Switchable Interlayer Magnetic Coupling of Bilayer CrI_3 . *Nanomaterials* **2021**, *11*, 2509.
- (18) Soriano, D.; Katsnelson, M. I.; Fernández-Rossier, J. Magnetic Two-Dimensional Chromium Trihalides: A Theoretical Perspective. *Nano Lett.* **2020**, *20*, 6225–6234.
- (19) Anderson, P. W. Antiferromagnetism. Theory of Superexchange Interaction. *Phys. Rev.* **1950**, *79*, 350–356.
- (20) Li, X.; Yu, H.; Lou, F.; Feng, J.; Whangbo, M.-H.; Xiang, H. Spin Hamiltonians in Magnets: Theories and Computations. *Molecules* **2021**, *26*, 803.

- (21) Beck, R. A.; Lu, L.; Sushko, P. V.; Xu, X.; Li, X. Defect-Induced Magnetic Skyrmion in a Two-Dimensional Chromium Triiodide Monolayer. *JACS Au* **2021**, *1*, 1362–1367.
- (22) Yamaguchi, K.; Takahara, Y.; Fueno, T. Ab-Initio Molecular Orbital Studies of Structure and Reactivity of Transition Metal-OXO Compounds. *Applied Quantum Chemistry*; Springer: Dordrecht, 1986; pp 155–184.
- (23) Pantazis, D. A. Meeting the Challenge of Magnetic Coupling in a Triply-Bridged Chromium Dimer: Complementary Broken-Symmetry Density Functional Theory and Multireference Density Matrix Renormalization Group Perspectives. *J. Chem. Theory Comput.* **2019**, *15*, 938–948.
- (24) Sharma, P.; Truhlar, D. G.; Gagliardi, L. Magnetic Coupling in a Tris-hydroxo-Bridged Chromium Dimer Occurs through Ligand Mediated Superexchange in Conjunction with Through-Space Coupling. *J. Am. Chem. Soc.* **2020**, *142*, 16644–16650.
- (25) Sivadas, N.; Okamoto, S.; Xu, X.; Fennie, C. J.; Xiao, D. Stacking-Dependent Magnetism in Bilayer CrI₃. *Nano Lett.* **2018**, *18*, 7658–7664.
- (26) Soriano, D.; Cardoso, C.; Fernández-Rossier, J. Interplay between interlayer exchange and stacking in CrI₃ bilayers. *Solid State Commun.* **2019**, *299*, 113662.
- (27) Jang, S. W.; Jeong, M. Y.; Yoon, H.; Ryee, S.; Han, M. J. Microscopic Understanding of Magnetic Interactions in Bilayer CrI₃. *Phys. Rev. Mater.* **2019**, *3*, No. 031001(R).
- (28) Pizzochero, M.; Yadav, R.; Yazyev, O. V. Magnetic exchange interactions in monolayer CrI₃ from many-body wavefunction calculations. *2D Mater.* **2020**, *7*, 035005.
- (29) Martin, R. L.; Illas, F. Antiferromagnetic Exchange Interactions from Hybrid Density Functional Theory. *Phys. Rev. Lett.* **1997**, *79*, 1539–1542.
- (30) Ruiz, E.; Alvarez, S.; Cano, J.; Polo, V. About the calculation of exchange coupling constants using density-functional theory: The role of the self-interaction error. *J. Chem. Phys.* **2005**, *123*, 164110.
- (31) Song, J.-W.; Giorgi, G.; Yamashita, K.; Hirao, K. Communication: Singularity-free Hybrid Functional with a Gaussian-attenuating Exact Exchange in a Plane-wave Basis. *J. Chem. Phys.* **2013**, *138*, 241101.
- (32) Ivády, V.; Armiento, R.; Szász, K.; Janzén, E.; Gali, A.; Abrikosov, I. A. Theoretical Unification of Hybrid-DFT and DFT+U Methods for the Treatment of Localized Orbitals. *Phys. Rev. B: Condens. Matter Mater. Phys.* **2014**, *90*, 035146.
- (33) Zhao, Q.; Kulik, H. J. Where Does the Density Localize in the Solid State? Divergent Behavior for Hybrids and DFT+U. *J. Chem. Theory Comput.* **2018**, *14*, 670–683.
- (34) Aras, M.; Kılıç, K. Combined Hybrid Functional and DFT+U Calculations for Metal Chalcogenides. *J. Chem. Phys.* **2014**, *141*, 044106.
- (35) Verma, P.; Truhlar, D. G. Does DFT+U Mimic Hybrid Density Functionals? *Theor. Chem. Acc.* **2016**, *135*, 182.
- (36) Perdew, J. P.; Burke, K.; Ernzerhof, M. Generalized Gradient Approximation Made Simple. *Phys. Rev. Lett.* **1996**, *77*, 3865–3868.
- (37) Perdew, J. P.; Burke, K.; Ernzerhof, M. Generalized Gradient Approximation Made Simple. *Phys. Rev. Lett.* **1996**, *77*, 3865.
- (38) Adamo, C.; Barone, V. Toward Reliable Density Functional Methods without Adjustable Parameters: The PBE0 Model. *J. Chem. Phys.* **1999**, *110*, 6158–6170.
- (39) Frisch, M. J.; Trucks, G. W.; Schlegel, H. B.; Scuseria, G. E.; Robb, M. A.; Cheeseman, J. R.; Scalmani, G.; Barone, V.; Petersson, G. A.; Nakatsuji, H.; Li, X.; Caricato, M.; Marenich, A. V.; Bloino, J.; Janesko, B. G.; Gomperts, R.; Mennucci, B.; Hratchian, H. P.; Ortiz, J. V.; Izmaylov, A. F.; Sonnenberg, J. L.; Williams-Young, D.; Ding, F.; Lipparini, F.; Egidi, F.; Goings, J.; Peng, B.; Petrone, A.; Henderson, T.; Ranasinghe, D.; Zakrzewski, V. G.; Gao, J.; Rega, N.; Zheng, G.; Liang, W.; Hada, M.; Ehara, M.; Toyota, K.; Fukuda, R.; Hasegawa, J.; Ishida, M.; Nakajima, T.; Honda, Y.; Kitao, O.; Nakai, H.; Vreven, T.; Throssell, K.; Montgomery, J. A., Jr.; Peralta, J. E.; Ogliaro, F.; Bearpark, M. J.; Heyd, J. J.; Brothers, E. N.; Kudin, K. N.; Staroverov, V. N.; Keith, T. A.; Kobayashi, R.; Normand, J.; Raghavachari, K.;